Program Digest, 2019 IEEE International Ultrasonics Symposium (IUS)
Glasgow, Scotland, October 6-9, 2019

Data-Driven Sensor Array Subsampling for Plane-Wave Ultrasound Imaging

Houssem Marzougui
Electrical and Computer Engineering Department
University of Victoria
Victoria, Canada
houssemmarzougui@uvic.ca

Daler Rakhmatov
Electrical and Computer Engineering Department
University of Victoria
Victoria, Canada
daler@ece.uvic.ca

***Abstract*—Ultrafast plane-wave ultrasound imaging offers very high frame rates but entails large volumes of backscattered data collected by sensor array over multiple plane-wave emissions at different angles. We propose a simple method for reducing the total amount of sampled data (subject to subsequent beamforming and coherent compounding). First, we acquire the zero-angle data in full, and then perform deterministic subsampling of the remaining nonzero-angle data. Our subsampling patterns are angle-specific and derived based on the zero-angle data.**

***Index Terms*—Plane-wave ultrasound imaging, coherent compounding, reduced data acquisition**

I. Introduction

Ultrafast plane-wave (PW) ultrasound imaging [1] typically involves acquiring a 3D raw dataset $\mathrm{RF}(t,x,\theta)$ by a transducer array, where θ denotes the steering angle of an emitted PW pulse (giving rise to the backscattered signals to be sampled), x refers to the individual sensor positions within the array, and t represents the sampling time instance. After beamforming and coherent compounding, we get a 2D compounded image dataset $D(z,x)$, where $z = ct/2$ is the imaging depth, and c is the speed of sound in the insonified medium.

Our objective is to reduce the amount of sensor array data recorded in $\mathrm{RF}(t,x,\theta)$, whose subsequent processing would still produce acceptable-quality $D(z,x)$. One way to achieve this goal is to use powerful techniques from the compressed sensing theory [2]. Briefly, to obtain an unknown data vector $\mathbf{u}$, we first acquire a smaller-sized vector of its measurements $\mathbf{v} = \mathbf{A}\mathbf{u} = \mathbf{A}\mathbf{\Phi}\mathbf{w}$, where (typically) $\mathbf{A}$ is a sub-Gaussian random matrix, and $\mathbf{\Phi}$ is some fitting orthonormal basis, such that $\mathbf{u} = \mathbf{\Phi}\mathbf{w}$ with $\mathbf{w}$ being sparse. We can then recover $\mathbf{u}$ by solving a suitable constrained optimization problem, e.g., $\arg\min \|\mathbf{w}\|_1$ subject to $\|\mathbf{A}\mathbf{\Phi}\mathbf{w}-\mathbf{v}\|_2 \le \epsilon$ for some $\epsilon > 0$. In this work, however, we explore a different approach that does not involve using $\mathbf{A}$, $\mathbf{\Phi}$, or iterative optimization. Instead, we first acquire zero-angle $\mathrm{RF}(t,x,\theta=0)$ in full, from which we derive deterministic subsampling patterns for the remaining nonzero-angle raw data. Next, we subsample $\mathrm{RF}(t,x,\theta \neq 0)$ accordingly, then beamform the acquired samples, and finally, compound the resulting beamformed data to produce $D(z,x)$.

This work was supported in part by the Natural Sciences and Engineering Research Council of Canada (NSERC).

Among various methods for computing $D(z,x)$, we focus on Fourier-domain image reconstruction [3]–[7]. Specifically, we shall make use of the zero-offset depth migration technique from our previous work [7], which is briefly outlined below. In the sequel, the f-axis, k_x-axis, and k_z-axis data refer to the outputs of the Fourier transform applied to the t-axis, x-axis, and z-axis data, respectively.

For each angle θ, we first transform the corresponding 2D raw data $\mathsf{P}_\theta(t,x)$ into its spectrum $\mathsf{F}_\theta(f,k_x)$.[1] Next, we remap the f-axis data into the k_z-axis data via linear interpolation, which yields the migrated spectrum $\mathsf{K}_\theta(k_z,k_x)$. Then, we transform the latter into its (k_z,x)-domain representation (via the inverse Fourier transform along the k_x-axis), and multiply the result element-wise by $\exp(j\pi k_z x \tan(\theta))$, thus producing the phase-shifted spectrum $\mathsf{S}_\theta(k_z,x)$. Finally, we compound all of such θ-specific spectra $\mathsf{S}_\theta(k_z,x)$ by adding them together (i.e., summing over a given set of θ values), and then apply the inverse Fourier transform along the k_z-axis to obtain $D(z,x)$. The spectral remapping step mentioned above is performed using the following formulas [7]:

$$\mathsf{K}_\theta(k_z,k_x) = A(k_z,k_x,\theta)\cdot \mathsf{F}_\theta\left(f_{\mathrm{mig}}(k_z,k_x,\theta),k_x\right), \qquad (1)$$

$$f_{\mathrm{mig}}(k_z,k_x,\theta) = \frac{ck_z}{1+\cos(\theta)}\left[1+(k_x/k_z)^2\right], \qquad (2)$$

$$A(k_z,k_x,\theta) = \frac{c}{1+\cos(\theta)}\left[1-(k_x/k_z)^2\right]. \qquad (3)$$

In the sequel, we shall focus on $\mathsf{H}(z,x)$, the complex-valued Hilbert transform of $D(z,x)$ (along the z-axis), which will be our desired output instead of $D(z,x)$.

II. Proposed Method

Let N_t, N_x, and N_a denote the number of sampling time instances, the number of sensors (channels), and the number of PW emission angles, respectively. The full acquisition of $\mathrm{RF}(t,x,\theta)$ would entail collecting as many as $N_t \times N_x \times N_a$ samples. We want to reduce the total number of acquired raw data samples, while still aiming to produce acceptable-quality compounded images.

[1]Note that $\mathsf{P}_\theta(t,x)$ is simply a 2D "slice" of $\mathrm{RF}(t,x,\theta)$ for a particular value of θ.

We begin the acquisition process by fully sampling the zero-angle 2D raw RF data $\mathsf{P}_0(t,x)$, i.e., our initial cost is $N_t \times N_x$ samples. Then, for each $\theta \neq 0$, we are to acquire some fraction $p < 1$ of the corresponding 2D raw RF data $\mathsf{P}_\theta(t,x)$. The total cost will become equal to $N_t \times N_x + p \times (N_t \times N_x) \times (N_a - 1)$ samples, which implies the savings of $\frac{1+p\times(N_a-1)}{N_a} \times 100\%$.

Let $\mathsf{P}^*_\theta(t,x)$ denote a subsampled representation of $\mathsf{P}_\theta(t,x)$, and let $\mathsf{M}_\theta(t,x)$ be a binary sampling matrix for $\mathsf{P}_\theta(t,x)$. If we have $\mathsf{M}_\theta(t_l,x_m) = 1$ for some specific location (t_l,x_m) within our sampling grid, then $\mathsf{P}^*_\theta(t_m,x_l) = \mathsf{P}_\theta(t_m,x_l)$; otherwise, $\mathsf{P}^*_\theta(t_m,x_l) = 0$. We express such subsampling compactly as $\mathsf{P}^*_\theta(t,x) = \mathsf{M}_\theta(t,x) \odot \mathsf{P}_\theta(t,x)$, where $\odot$ denotes the element-wise multiplication. The total number of ones in $\mathsf{M}_\theta(t,x)$ must be equal to $N_p = p \times (N_t \times N_x)$.

Given multiple θ-specific $\mathsf{P}^*_\theta(t,x)$ as inputs, we apply our Fourier-domain reconstruction sequence from [7] to all of them individually, which is then followed by compounding (over all nonzero θ values) and the Hilbert transform computations:

$$\mathsf{P}^*_\theta(t,x) \to \mathsf{F}^*_\theta(f,k_x) \to \mathsf{K}^*_\theta(k_z,k_x) \to \mathsf{S}^*_\theta(k_z,x),$$
$$\sum_{\theta\neq 0} \mathsf{S}^*_\theta(k_z,x) \to \mathsf{H}^*(z,x).$$

The zero-angle data $\mathsf{P}_0(t,x)$, acquired in full, yields

$$\mathsf{P}_0(t,x) \to \mathsf{F}_0(f,k_x) \to \mathsf{K}_0(k_z,k_x) \to \mathsf{S}_0(k_z,x) \to \mathsf{H}_0(z,x).$$

Finally, our target output $\mathsf{H}(z,x)$ is estimated as follows:

$$\widehat{\mathsf{H}}(z,x) = \mathsf{H}^*(z,x) + \mathsf{H}_0(z,x) + \widetilde{\mathsf{H}}(z,x), \qquad (4)$$

where $\widetilde{\mathsf{H}}(z,x)$ serves as an auxiliary "data filler" to mitigate the negative impact of subsampling. In the worst case, $\widetilde{\mathsf{H}}(z,x)$ is simply all zeros. In the best case, it provides an adequate approximation of unknown $\overline{\mathsf{H}}^*(z,x)$ that represents what we would have obtained from the missing data:

$$\overline{\mathsf{P}}^*_\theta(t,x) \to \overline{\mathsf{F}}^*_\theta(f,k_x) \to \overline{\mathsf{K}}^*_\theta(k_z,k_x) \to \overline{\mathsf{S}}^*_\theta(k_z,x),$$
$$\sum_{\theta\neq 0} \overline{\mathsf{S}}^*_\theta(k_z,x) \to \overline{\mathsf{H}}^*(z,x),$$

where each "hypothetical" $\overline{\mathsf{P}}^*_\theta(t,x)$ contains the data samples from $\mathsf{P}_\theta(t,x)$ that are not in $\mathsf{P}^*_\theta(t,x)$. Equivalently, $\overline{\mathsf{P}}^*_\theta(t,x) = \overline{\mathsf{M}}_\theta(t,x) \odot \mathsf{P}_\theta(t,x)$, where $\overline{\mathsf{M}}_\theta(t,x)$ is the complemented version of binary $\mathsf{M}_\theta(t,x)$. Since $\overline{\mathsf{P}}^*_\theta(t,x) = \mathsf{P}_\theta(t,x) - \mathsf{P}^*_\theta(t,x)$, we get $\mathsf{H}(z,x) - \widehat{\mathsf{H}}(z,x) = \overline{\mathsf{H}}^*(z,x) - \widetilde{\mathsf{H}}(z,x)$, which stresses the importance of $\widetilde{\mathsf{H}}(z,x)$ being close to unknown $\overline{\mathsf{H}}^*(z,x)$.

The main idea of this work pertains to the derivation of the θ-specific sampling pattern matrices $\mathsf{M}_\theta(t,x)$ from the zero-angle information stored in $\mathsf{P}_0(t,x)$. The first step is to identify which N_p data samples in $\mathsf{P}_0(t,x)$ are deemed most useful: for example, we may select those having the largest absolute values. Next, we record their corresponding locations as ones in our initial zero-angle matrix $\mathsf{M}_0(t,x)$, and then generate its (k_z,x)-domain representation denoted by $\mathsf{S}^\mathsf{M}_0(k_z,x)$:

$$\mathsf{M}_0(t,x) \to \mathsf{F}^\mathsf{M}_0(f,k_x) \to \mathsf{K}^\mathsf{M}_0(k_z,k_x) \to \mathsf{S}^\mathsf{M}_0(k_z,x). \qquad (5)$$

For any given $\theta \neq 0$, the binary sampling matrix $\mathsf{M}_\theta(t,x)$ can now be obtained from $\mathsf{S}^\mathsf{M}_0(k_z,x)$ as follows. We multiply $\mathsf{S}^\mathsf{M}_0(k_z,x)$ element-wise by $\exp(-j\pi k_z x \tan(\theta))$, transform it into its (k_z,k_x)-domain version, and perform demigration (i.e., we remap from f_{mig} back to f), thus producing a particular θ-specific (f,k_x) spectrum. Then, we apply the inverse Fourier transform to the said spectrum, which yields the desired (t,x)-domain matrix $\widetilde{\mathsf{M}}_\theta(t,x) \approx \mathsf{M}_\theta(t,x)$. To get our final $\mathsf{M}_\theta(t,x)$, we simply binarize $\widetilde{\mathsf{M}}_\theta(t,x)$ via thresholding: for example, the first N_p largest-magnitude elements of $\widetilde{\mathsf{M}}_\theta(t,x)$ become 1, while the rest are set to 0. Essentially, $\mathsf{S}^\mathsf{M}_0(k_z,x)$ goes through the reconstruction sequence (5) in reverse, except that $\theta \neq 0$ is now incorporated into the corresponding remapping equations.

III. Evaluation Results

To evaluate our proposed subsampling method, we have used two experimental datasets from PICMUS-2017 [8], corresponding to $N_a = 5$ PW emissions (5.208-MHz frequency, 67% bandwidth, 2.5-cycle excitation) at $-16°$, $-8°$, $0°$, $+8°$, and $+16°$. These datasets, referred to as Type-1 and Type-2, were recorded by a 128-element 38.4-mm linear probe, whose sampling frequency was set to 20.832 MHz [8]. For each θ, the N_t-by-N_x size of raw RF data frames was 1536×128. After reconstruction, we generated the B-mode images by log-compressing their respective normalized envelope sections covering the z-axis range $[5, 50]$ mm, as shown in Fig. 1.

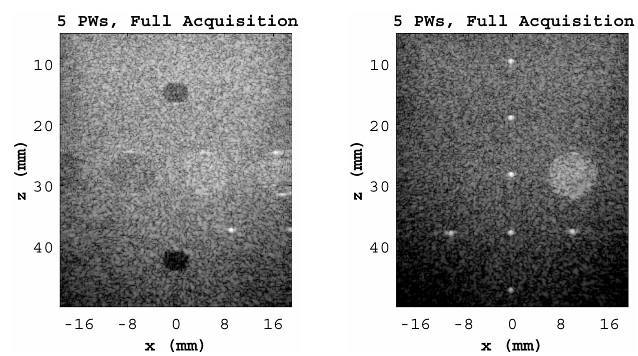

Fig. 1. Reference Type-1 (left) and Type-2 (right) compounded images.

Fig. 2 illustrates the effect of subsampling applied to the $16°$-angle Type-2 raw RF data frame. The top part of Fig. 2 shows the grayscale image of the absolute values of $\mathsf{P}_\theta(t,x)$ elements (100% RF data), while the bottom part shows the corresponding image of $\mathsf{P}^*_\theta(t,x)$ for $p = 0.03$ (3% RF data). Note that we were able to capture many large-magnitude samples, whose locations were specified in advance by $\mathsf{M}_\theta(t,x)$ derived from $\mathsf{S}^\mathsf{M}_0(k_z,x)$ for $\theta = +16°$. Recall that $\mathsf{S}^\mathsf{M}_0(k_z,x)$ itself is generated from $\mathsf{M}_0(t,x)$. In this work, we obtain $\mathsf{M}_0(t,x)$ from the initial zero-angle RF data $\mathsf{P}_0(t,x)$ acquired in full: we simply identify the locations of the first $N_{p=0.03}$ largest-magnitude samples in $\mathsf{P}_0(t,x)$, and then set the corresponding elements in $\mathsf{M}_0(t,x)$ to 1 (with the others made equal to 0).

Table I provides the quantitative quality indicators for the Type-1 and Type-2 images under consideration. These metrics have been computed using the original PICMUS-provided

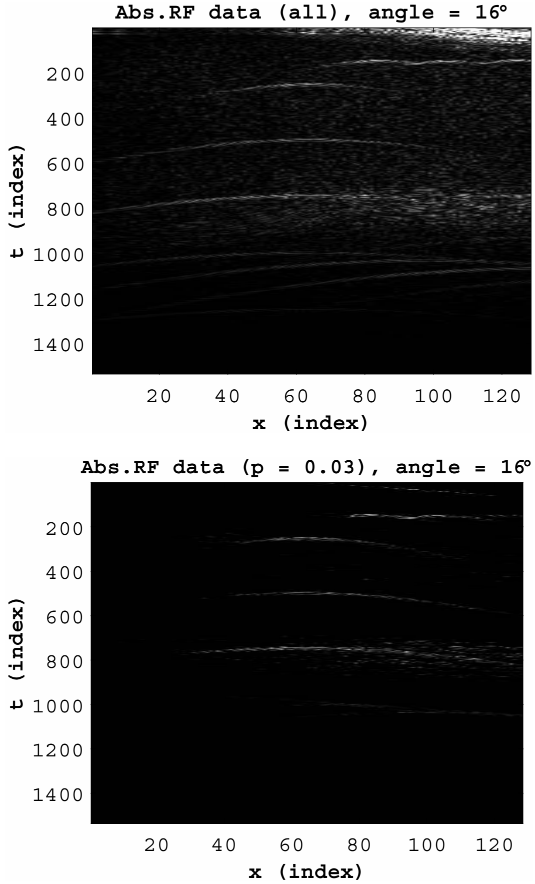

Fig. 2. Subsampling illustration: TYPE-2 RF data, $\theta = +16°$, $p = 0.03$.

evaluation routines [8]. The TYPE-1 images are assessed based on the contrast-to-noise ratios (CNR, dB) for the top/bottom cyst phantoms (two anechoic cylinder targets), as well as the axial/lateral full widths at half-maximum (FWHM, mm) for the bottom-right point phantom (a wire target). The TYPE-2 images are assessed based on the average axial/lateral $\overline{\text{FWHM}}$, computed over all seven point phantoms.

In this work, we report the following cases of subsampling $N_a - 1 = 4$ nonzero-angle raw RF data frames:

A) $p = 0.01$, resulting in 79.2% overall savings;
B) $p = 0.03$, resulting in 77.6% overall savings;
C) $p = 0.09$, resulting in 72.8% overall savings.

Note that our initial (full) acquisition of the zero-angle data incurs the immediate cost of $N_t \times N_x$ samples, which amounts to 20% with respect to their total number $(N_t \times N_x) \times N_a$. In all cases, we let

$$\widetilde{\mathsf{H}}(z,x) = \frac{\|\mathsf{H}^*(z,x) + \mathsf{H}_0(z,x)\|_2}{\|\mathsf{H}_0(z,x)\|_2} \cdot \overline{\mathsf{H}}_0^*(z,x), \qquad (6)$$

where $\overline{\mathsf{H}}_0^*(z,x)$ denotes the reconstruction result for the input $\overline{\mathsf{P}}_0^*(t,x) = \overline{\mathsf{M}}_0(t,x) \odot \mathsf{P}_0(t,x)$ that simulates the "missing" portion of the initial zero-angle raw RF data frame (i.e., as if it underwent $\mathsf{M}_0(t,x)$-based subsampling). The multiplication factor in (6) accounts for the energy content difference arising due to compounding.

TABLE I
ACQUISITION COST AND RESULTING IMAGE QUALITY INDICATORS.

Case	Acq. Cost (%)	TYPE-1 Top/Bottom CNR (dB)	TYPE-1 Axial/Lateral FWHM (mm)	TYPE-2 Axial/Lateral $\overline{\text{FWHM}}$ (mm)
5PW	100	8.0/9.5	0.49/0.48	0.47/0.44
1PW	20.0	8.6/6.0	0.48/0.85	0.48/0.80
A	20.8	8.4/6.0	0.46/0.79	0.46/0.68
B	22.4	6.1/6.0	0.46/0.64	0.47/0.60
C	27.2	3.5/6.2	0.47/0.60	0.46/0.55

Fig. 3 shows the images available after the initial acquisition of the zero-angle RF data frame. Acquiring additional four nonzero-angle RF data frames in full would yield the compounded images seen in Fig. 1. Comparing the 1-PW and 5-PW entries in Table I, it is reasonable to anticipate that compounding zero-angle full-input reconstruction data with nonzero-angle partial-input reconstruction data would produce the top and bottom CNR values within $[8.0, 8.6]$ and $[6.0, 9.5]$ dB, respectively; we would also expect the lateral FWHM values to decrease from 0.80-0.85 towards 0.44-0.48 mm.

Table I and Fig. 4, 5, and 6 confirm the expected FWHM improvement (down to 0.55-0.60 mm), but the overall contrast performance is actually much worse than anticipated.[2] This discrepancy can be attributed to the fact that our current approach favors large-magnitude samples, thus aiming to capture signals from strong reflectors, such as wire targets. Formation of the image portions containing weak reflectors and anechoic targets is done mostly by $\mathsf{H}_0(z,x)$ and $\widetilde{\mathsf{H}}(z,x)$. Our current choice of $\widetilde{\mathsf{H}}(z,x)$ appears to be inadequate for the TYPE-2 images (in terms of the CNR values obtained), meaning that further investigations into enhanced $\widetilde{\mathsf{H}}(z,x)$ are needed.

REFERENCES

[1] M. Tanter and M. Fink, "Ultrafast imaging in biomedical ultrasound," *IEEE Trans. Ultrason., Ferroelect., Freq. Contr.*, vol. 61, no. 1, pp. 102–119, Jan 2014.
[2] Y. Eldar, *Sampling Theory*. NY: Cambridge, 2015.
[3] J. Cheng and J. Lu, "Extended high-frame rate imaging method with limited-diffraction beams," *IEEE Trans. Ultrason., Ferroelect., Freq. Contr.*, vol. 53, no. 5, pp. 880–899, May 2006.
[4] D. Liu and T. Ji, "Plane wave image formation in spatial-temporal frequency domain," in *Proc. IEEE International Ultrasonics Symposium*, Sep 2016, pp. 1–5.
[5] D. Garcia, L. Tarnec, S. Muth, E. Montagnon, J. Poree, and G. Cloutier, "Stolt's f-k migration for plane wave ultrasound imaging," *IEEE Trans. Ultrason., Ferroelect., Freq. Contr.*, vol. 60, no. 9, pp. 1853–1867, Sep 2013.
[6] A. Besson, M. Zhang, F. Varray, H. Liebgott, D. Friboulet, Y. Wiaux, J. Thiran, R. Carrillo, and O. Bernard, "A sparse reconstruction framework for Fourier-based plane-wave imaging," *IEEE Trans. Ultrason., Ferroelect., Freq. Contr.*, vol. 63, no. 12, pp. 2092–2106, Dec 2016.
[7] M. Albulayli and D. Rakhmatov, "Fourier-domain depth migration for plane wave ultrasound imaging," *IEEE Trans. Ultrason., Ferroelect., Freq. Contr.*, vol. 65, no. 8, pp. 1321–1333, Aug 2018.
[8] CREATIS, "Plane-wave Imaging Challenge in Medical UltraSound (PICMUS): Algorithm Evaluation Framework." [Online]. Available: https://www.creatis.insa-lyon.fr/EvaluationPlatform/picmus/

[2]We should also mention that in all cases the resulting images did pass the Kolmogorov-Smirnov tests for speckle preservation [8].

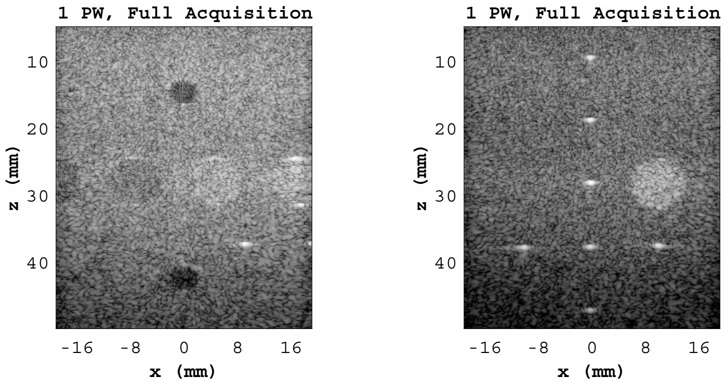

Fig. 3. Initial zero-angle images: single PW emission at $\theta = 0$.

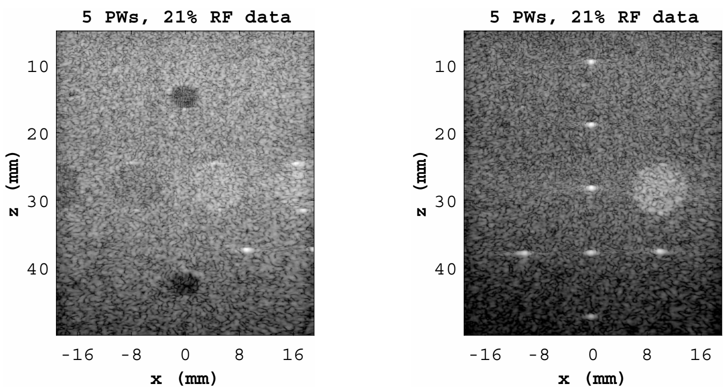

Fig. 4. Compounded images: nonzero-angle RF data subsampling, $p = 0.01$ (case A).

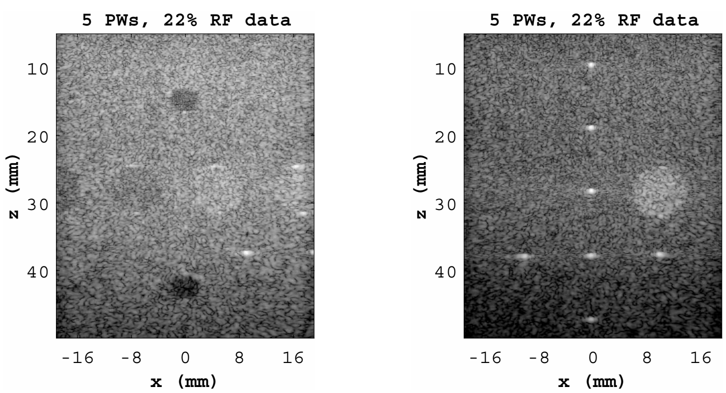

Fig. 5. Compounded images: nonzero-angle RF data subsampling, $p = 0.03$ (case B).

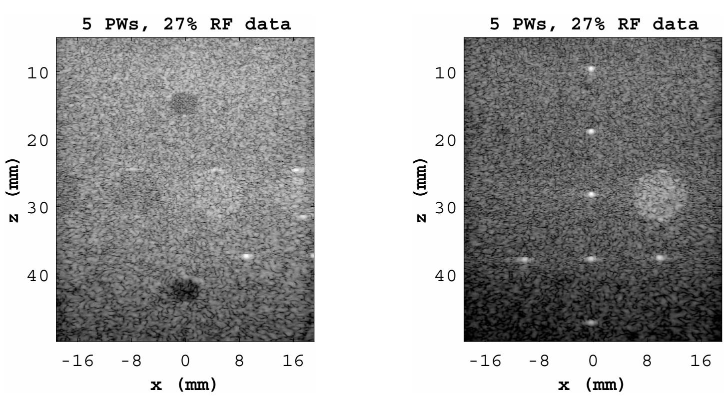

Fig. 6. Compounded images: nonzero-angle RF data subsampling, $p = 0.09$ (case C).